RESEARCH | Article in Press

mregDCs preferentially associate with regulatory T cells in the pancreatic tumor microenvironment

Yanyun Hao · Oshri Yosefov-Levi · Sebastian Arcila-Barrera · Yehuda Shovman · Avital Sarusi-Portuguez · Vladyslav Holiar · Hasan Burak Kunukcu · Moshe Biton · William L. Hwang · Jinke Cheng · Sharona Tornovsky-Babeay · Oren Parnas

Received: 17 April 2026 / Accepted: 10 October 2026
© The Author(s) 2026

Abstract

Two major, contradictory forces act simultaneously on immune cells in the tumor microenvironment (TME): one enhances the immune response following the identification of danger, while the other protects the tumor by imposing an immunosuppressive environment. The interactions between immune cells in the TME are therefore critical for the ability to mount an effective immune response and for the outcome of related therapies. Here, we use single-cell RNA-seq and spatial transcriptomics to investigate cellular interactions in pancreatic cancer. We identify close interactions between regulatory T cells (Tregs) and dendritic cells (DCs) and reveal potential cytokines that mediate these interactions. Experiments using differentiated DCs and Tregs show that Tregs induce the mature mregDC state, and that mregDCs, in turn, enhance Treg proliferation and activation. Together, these data suggest that DC–Treg proximity fuels a reinforcing feedback loop that may support the immunosuppressive TME in pancreatic cancer, and that blocking IL15 and Tnfsf11—the cytokines that mediate this signaling—may disrupt DC–Treg interactions while sparing CD8 T-cell activation in the TME.

Introduction

Pancreatic ductal adenocarcinoma (PDAC) is a highly lethal malignancy, with a five-year survival rate of only 13% [1, 2]. Currently available treatments, including chemotherapy and radiation, result in only a modest increase in survival. Despite late detection, pancreatic cancer develops over a period of 10–15 years [3]. During this extended phase, epithelial cells accumulate mutations and eventually undergo malignant transformation [4]. In parallel, immune cells are recruited to the pancreas and progressively alter their gene expression and cellular states in response to signals from the evolving microenvironment [5]. Notably, up to 80% of pancreatic tumor mass is composed of non-malignant stromal and immune cells [6, 7]. Regardless of the substantial infiltration of immune cells into the tumor, immunotherapy has shown limited benefit in PDAC and is therefore not currently used for PDAC patients. Immunosuppression mediated by several immune cell populations is a major contributor to this failure.

This Article in Press is shared early to give you faster access to new research. It is citable and carries a permanent DOI. The final edited version will replace it automatically.

Published online: 20 October 2026

Regulatory T cells (Tregs), which play essential roles in maintaining peripheral tolerance [8, 9], have been shown to promote immunosuppression and are associated with poor survival in many cancer types. In PDAC, Tregs have been shown to enhance immunosuppression and support tumor growth [10], although other work suggests that Tregs may also suppress myeloid-derived suppressor cells and therefore have an anti-tumor effect [11]. These contradictory findings imply that the interactions between Tregs and other immune or stromal cells critically shape Treg function in PDAC.

Dendritic cells (DCs) are central antigen-presenting cells that prime T cells in the lymph nodes (LNs), delivering multiple instructive signals through cytokines and surface receptors. At least some of these signals are required for activation of effector T cells in peripheral tissues [12]. Several DC subtypes were detected in the TME of multiple cancer types, including plasmacytoid DCs (pDCs), conventional DC1 (cDC1; $Xcr1^+$), conventional DC2 (cDC2; $CD209a^+$), and mature DCs enriched for immunoregulatory and migratory molecules (mregDCs; $Fscn1/Ccr7^+$) [13, 14]. Previous studies have shown that DCs interact with both $CD8^+$ T cells and Tregs within the tumor microenvironment (TME). Following subcutaneous injection of cancer cell lines into syngeneic mice, cDCs recruit and activate Tregs in the TME, and these interactions can compete with DC–$CD8^+$ T-cell interactions, thereby limiting effective antitumor immunity [15, 16]. Additionally, You et al. recently demonstrated that Tregs interact with mregDCs in a mouse model of colorectal cancer, and that the abundance of Tregs and mregDCs correlates with patient survival in human cancer [17] and mregDC abundance predicts improved progression-free survival in melanoma patients treated with immune checkpoint inhibitors (ICIs) [18], while mregDC1s drive the activation of $CD8^+$ T cells in vitro [19]. Consistently, intratumoral niches containing mregDCs regulate the differentiation and activation of tumor-specific $CD8^+$ T cells following ICI therapy [20, 21].

Importantly, DCs are less abundant in the PDAC TME compared to lung adenocarcinoma, and increasing DC numbers using FLT3L in combination with ICIs [22, 23] can enhance effective antitumor immunity. Thus, DC–Treg interactions are generally considered to promote immunosuppression, whereas DC–$CD8^+$ T-cell interactions, especially in the context of ICI therapy, promote antitumor responses. However, prior studies typically examined only a single DC and T-cell subset pair. As a result, the broader landscape of DC–T-cell interactions, their bidirectional effects, and their relevance to PDAC remain poorly defined. Furthermore, the abundance and function of DC subtypes differ markedly between PDAC and other cancers, complicating the extrapolation of findings.

Here, we use single-cell RNA sequencing (scRNA-seq) and spatial transcriptomics to identify the key relevant interactions between immune and stromal cells in PDAC, and subsequently investigate the functional consequences of these interactions using in vitro differentiated cells. We reveal a self-amplifying circuit that potentially enhances PDAC immunosuppression.

Methods

Animals and housing conditions

All animal experiments were performed according to the protocols approved by the Joint Ethics Committee (Institutional Animal Care and Use Committee) of the Hebrew University (Jerusalem, Israel) and Hadassah Medical Center (Jerusalem, Israel). All our animal-handling procedures were performed according to the National Institutes of Health and Institutional guidelines, with approval from the Institutional Animal Care and Use Committee of the Hebrew University (Jerusalem, Israel). The ethics protocol for mouse holding and the experimental procedures are MD-22-16651-5 and MD-22-16958-1.

The following mouse strains were purchased from the Jackson Laboratory: B6.Cg-Tg (Tcra Tcrb) 425Cbn/J (strain #:004194), B6N.129(B6J)-Gt(ROSA)26Sor$^{tm1(CAG-cas9*,-EGFP)Fezh}$/J (strain #:026556), B6.129(Cg)-Foxp3$^{tm3(HBEGF/GFP)Ayr}$/J mice (strain #:016958). The C57BL/6 mice (six weeks) were purchased from Envigo

Israel. The animals were housed and maintained under SPF conditions in facilities and treated humanely throughout the studies.

Cell lines and culture conditions

KPCY mouse pancreatic cancer cell line (6499c4) was purchased from Kerafast Inc. (Cat. # EUP015-FP), and maintained in DMEM medium supplemented with 10% FBS and 1% sodium pyruvate.

We generated an additional mouse tumor-derived cell line from tumors arising in Ptf1a-CreER; $Trp53^{fl/fl}$; LSL-$Kras^{G12D}$ (PRTP) mice. Spatial transcriptomic analysis of tumors generated following orthotopic transplantation of these cells is presented in Supplementary Figure 9. 293T cells (ATCC CRL-3216) were maintained in DMEM medium supplemented with 10% FBS and 1% sodium pyruvate. These adherent cells were passaged every 3 days using Trypsin–EDTA (0.25%).

In vitro generation of iTreg

To generate iTregs, we removed the spleen of eight-week-old female mice and ground it into cell suspensions. Red blood cells were removed using red blood cell lysis buffer. $CD4^+$ T cells were isolated from the spleen according to the EasySep Mouse $CD4^+$ T Cell Isolation Kit protocol (STEMCELL). T cells were cultured in RPMI 1640 media supplemented with 10% heat-inactivated FBS, β-mercaptoethanol,1% L-glutamine, 1% penicillin/streptomycin, 1% MEM non-essential amino acids, 1% HEPES, and 1% sodium pyruvate. Treg cells were induced by adding anti-CD3 (1 µg/mL), anti-CD28 (1 µg/mL), IL-2 (10 ng/mL), TGF-β1 (5 ng/mL), purified anti-mouse IFN-γ antibody (1 µg/mL), and purified anti-mouse IL-4 antibody (1 ug/mL) to the culture medium and culturing at 37 degrees for 4 days.

Differentiation of bone marrow-derived dendritic cells (BMDCs)

To obtain BMDCs, femurs and tibiae were removed from eight-week-old female mice, and the bone marrow was flushed. Red blood cells were lysed using red blood cell lysis buffer. For GM-CSF-induced DCs, bone marrow cells were plated in 100 mm diameter dishes (untreated) at a concentration of 2×10^5 per mL in 10 mL of DC medium. The basic DC medium is the same as T cell media. Murine GM-CSF (20 ng/ml) was added on day 0. On day two of the culture, 10 ml of fresh medium supplemented with GM-CSF was added. On day 5, 10 mL of medium was gently removed and 10 mL of fresh medium with GM-CSF was added. On day 7, 5 mL of fresh medium with GM-CSF was added to the cells, and on day 8, floating cells were recovered and used for downstream applications. For FLT3L-induced DCs, bone marrow cells were plated in 100 mm diameter dishes (untreated) at a concentration of 1.5×10^6 per mL in 10 mL of DC medium. Mouse Flt-3 Ligand (FLT3L) (100 ng/mL) was added on day 0. On day 3 of the culture, 1ug of FLT3L was added to each 100 mm diameter dish. On day 7 of the culture, 10 ml of fresh medium supplemented with FLT3L (100 ng/mL) was added. On day 8 of culture, the DCs were stimulated, and flow cytometry was performed on day 9. Cells were maintained at 37 °C in a 5% CO2-humidified atmosphere.

Flow cytometry staining for surface and intracellular transcription factor detection

For cell surface staining, antibodies were dissolved in FACS buffer (PBS solution containing 2% FBS) at a ratio of 1:200 to prepare a surface antibody cocktail. The cells were mixed with the surface antibody and incubated at 4 °C in the dark for 30 min. The cells were washed with FACS buffer and centrifuged at 400 × g for 5 min, discarding the supernatant. Finally, the cells were resuspended in FACS buffer for flow cytometry analysis. For intracellular protein staining, after surface antibody staining, cells were permeabilized and fixed using the

True-Nuclear™ transcription factor buffer kit (BioLegend) according to the manufacturer's instructions for intracellular protein staining.

Lentiviral production and transduction

Lentiviral particles were generated using HEK293T cells, following the method previously described [24]. Briefly, cells were transfected using polyethylenimine (PEI) as the transfection reagent. The vector, packaging (pCMVΔR8.2; Addgene #12263), and envelope (pCMV-VSV-G; Addgene #8454) plasmids were mixed at a ratio of 4:3:1, respectively. PEI (3 µg/µL) was added at 0.7 µL per µg of total DNA following dilution of DNA and PEI in Opti-MEM. After a 15-min incubation at room temperature, the DNA–PEI complex was added to the cells. Twelve hours post-transfection, the medium was replaced with enriched DMEM containing 10% FCS, sodium pyruvate, non-essential amino acids, and L-glutamine. Viral supernatants were collected 48 and 72 h after transfection and filtered through a 0.45 µm PES membrane. Viral particles were concentrated by high-speed centrifugation (14,000 rpm, 3 h, 10 °C). Pellets were resuspended in sterile PBS, aliquoted, and stored at − 80°C.

In vitro viral transduction of Treg cells

In vitro-induced Treg cells were generated as described above. Following activation with plate-bound anti-CD3 and soluble anti-CD28 antibodies, cells were cultured for 4 h at 37 °C in a humidified incubator containing 5% CO_2. Viral supernatant was then added to the cultures (20 µL concentrated viral particles per 96-well), and cells were maintained under Treg-polarizing conditions for 5 days. Transduction efficiency was assessed by flow cytometry on day 5 following viral infection (The cartoon illustration is shown in Fig. 4F).

IL-15 stimulation of Treg cells

Day-5 iTreg cells were harvested, washed, and resuspended in fresh Treg medium. Cells were seeded into 96-well U-bottom plates at 1×10^5 cells per well and stimulated with recombinant mouse IL-15 (20 ng/mL) for 3 days. Following stimulation, cells were collected and analyzed by flow cytometry for the expression of CTLA-4 and CD25 (The cartoon illustration is shown in Supplementary Fig. 10A).

BMDC stimulation assays

FLT3L-derived BMDCs were generated as described above and harvested on day 8 of differentiation. Cells were seeded at 1×10^6 cells/mL in 12-well plates and stimulated for 24 h with recombinant cytokines, Treg-conditioned medium, or Treg co-culture as indicated in each experiment. The following cytokines were used at the indicated concentrations: IFN-γ (20 ng/mL), TNFSF11 (20 ng/mL), TGF-β1 (5 ng/mL), IL-2 (10 ng/mL), IL-4 (10 ng/mL), IL-6 (10 ng/mL), IL-10 (10 ng/mL), IL-12 (10 ng/mL), IL-23 (10 ng/mL), and IL-33 (10 ng/mL). Lipopolysaccharide (LPS; 100 ng/mL) was used as a positive control where indicated. Following stimulation, BMDCs were analyzed by flow cytometry for CCR7 and PD-L1 expression.

Isolation and culture of Foxp3-GFP$^+$ Treg cells

Spleens were collected from Foxp3-GFP reporter mice and processed into single-cell suspensions. $CD4^+$ T cells were enriched using a CD4 T-cell isolation kit and stained with antibodies against CD4 and CD25. $CD4^+CD25^+GFP^+$ Treg cells were sorted by FACS. Sorted Treg cells were cultured in Treg medium supplemented with IL-2 for 5 days. Culture supernatants were collected, centrifuged, and filtered through a 0.22-µm filter prior to use. Cells were harvested and resuspended at 1×10^6 cells/mL for subsequent experiments (The cartoon illustration is shown 1 Shown in Fig. 3G).

Treg–BMDC co-culture assays

FLT3L-derived BMDCs were generated from C57BL/6 mice as described above. For direct co-culture experiments, BMDCs and Foxp3-GFP$^+$ Treg cells were cultured at a ratio of 1:5 (1×10^5 BMDCs and 5×10^5 Tregs per well) for 24 h. For conditioned-medium experiments, BMDCs were cultured in the presence of Treg-conditioned medium for 24 h. Untreated BMDCs cultured in DC medium alone served as controls. Following treatment, BMDCs were analyzed by flow cytometry for CCR7 and PD-L1 expression (The cartoon illustration is shown in Fig. 3A).

Treg proliferation assay

FLT3L-derived BMDCs were pulsed with OVA323–339 peptide for 6 h and subsequently cultured with Treg-conditioned medium for an additional 18 h. Control BMDCs received DC medium alone.

OT-II-derived Treg cells were generated in vitro and labeled with carboxyfluorescein succinimidyl ester (CFSE; 5 μM) according to the manufacturer's instructions. CFSE-labeled OT-II Tregs were co-cultured with OVA-loaded BMDCs at a ratio of 5:1 for 4 days. Following co-culture, cells were harvested and analyzed by flow cytometry. Treg proliferation was determined by CFSE dilution, and the expression of activation markers was assessed by antibody staining (The cartoon illustration is shown in Fig. 5B).

Orthotopic transplantation of 6499c4 and PRTP cells in C57BL/6 mice

Orthotopic pancreatic tumors were established by transplanting 6499c4 or PRTP cells [25] into the pancreas of six-week-old female C57BL/6 mice. Briefly, 6499c4 or PRTP cells were harvested, washed twice with PBS, and resuspended at a concentration of 5×10^5 cells per 25 μL. The cell suspension was mixed 1:1 with Matrigel (Corning) and kept on ice until it was injected. Mice were anesthetized, and a small incision was made in the subsplenic region to expose the spleen and pancreas. 50 μL of the 6499c4 or PRTP cell–Matrigel mixture was slowly injected into the pancreatic capsule using a 0.5 ml insulin syringe. The incision was then closed with surgical sutures, and the mice were placed under a warming lamp until recovery from anesthesia. 12 days after transplantation, palpable or visible tumor nodules were observed beneath the spleen, confirming successful establishment of orthotopic pancreatic tumors.

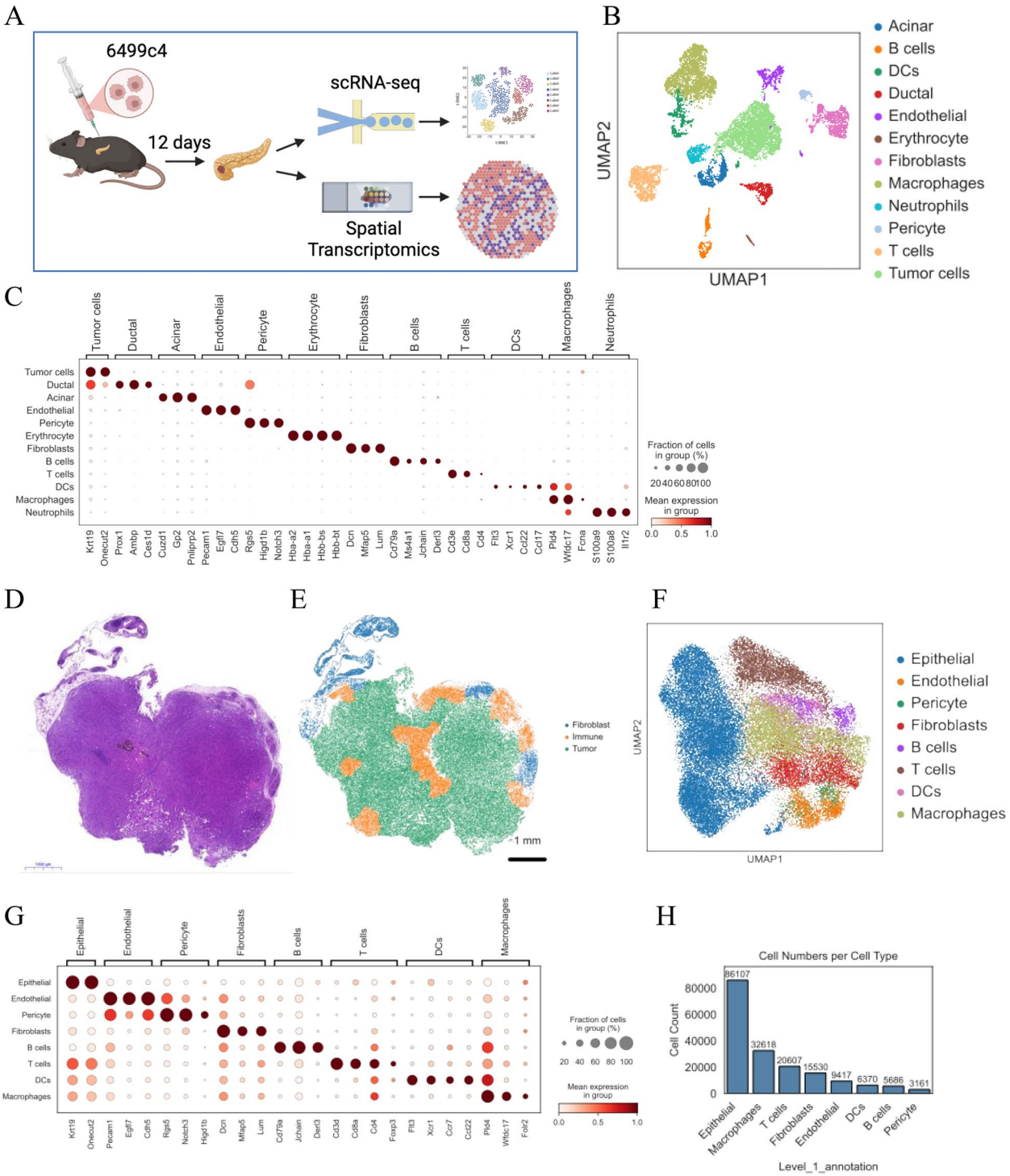
Tumor tissue processing for spatial transcriptomics and single-cell RNA sequencing

Pancreatic tumors were generated by orthotopic transplantation of the 6499c4 or PRTP pancreatic cancer cell line into six-week-old female C57BL/6 mice as described above. Mice were euthanized 12 days post-transplantation, and tumors were excised and rinsed with 1 × HBSS supplemented with 10% FBS. The same tumor was divided for spatial transcriptomics and single-cell RNA sequencing (scRNA-seq) analyses.

For spatial transcriptomics, samples were fixed in 4% paraformaldehyde for 1 h, followed by dehydration in 70% ethanol at 4 °C overnight. The dehydrated tissues were embedded in paraffin, and paraffin blocks were sent to Vizgen Inc. Two serial sections of 10 microns were taken, one for hematoxylin and eosin (H&E) staining and the second for MERFISH using a predesigned custom panel of 183 genes. A MERSCOPE gene panel was designed using Vizgen's Gene Panel Design Portal (https://vizgen.com/gene-panel/).

For scRNA-seq, we followed our previously published protocol [5, 26].

We used Chromium Single Cell 3′ Reagent Kit nextGEM (10 × Genomics) and prepared libraries for sequencing following the manufacturer's instructions. Sequencing on Illumina Nova-seq was performed with the following read length: 28 bp (Read1) and 90 bp (Read2).



Spatial transcriptomics data processing and analysis

Data processing and analysis were performed primarily using the Scanpy (v1.10) and Squidpy (v1.6) frameworks, following standard workflows. Raw data were obtained from Vizgen MERSCOPE outputs, consisting of a gene expression matrix (cell_by_gene.csv) and a corresponding metadata file (cell_metadata.csv) containing spatial coordinates and morphological information. Quality control (QC) was performed, and cells with fewer than 20 detected transcripts were excluded from further analysis to ensure data quality and consistency. For

Fig. 1 Single-cell RNA-seq and spatial transcriptomics reveal the population of cells in a pancreatic tumor. **A** Schematic overview of the experimental workflow. 6499c4 pancreatic cancer cells were orthotopically injected into the pancreas of syngeneic C57BL/6 mice. Twelve days post-injection, tumors were harvested and processed for single-cell RNA sequencing (scRNA-seq) and spatial transcriptomics. **B** UMAP of scRNA-seq data showing the main cell populations in orthotopic PDAC tumors. **C** Dot plot displaying representative marker genes used to annotate the main cell populations in the scRNA-seq data. **D** Hematoxylin and eosin (H&E) staining of the formalin-fixed PDAC tumor section used for spatial transcriptomics. The bar plot is 1mm. **E** Serial section of the slice shown in **D**, used for spatial transcriptomics. Three major cellular hubs were identified within the PDAC tumor section: a malignant-enriched hub, stromal regions enriched for fibroblasts, and an immune-enriched hub. The bar plot is 1mm. **F** UMAP of spatial transcriptomics data showing major cell types within the tumor section. **G** Dot plot showing representative marker genes used to annotate the cell types in the spatial transcriptomics data. **H** Bar plot showing the number of cells of each type in the spatial transcriptomics data. Unannotated cells were excluded from the graph and downstream analyses

normalization, gene counts were normalized to a target sum of 10^4, and a log1p transformation was applied. For dimension reduction, principal component analysis (PCA) was performed. Then, a nearest-neighbor graph was constructed, followed by Leiden clustering based on a 15-nearest-neighbor graph to identify different cell populations in the transcriptome.

The cell types, as shown in Fig. 1B and F, were assigned using known markers. To assign each cell subpopulation, we used gene signatures. Signatures were calculated using UCell [27]. The relevant signatures were compared for each cell subset, and the difference between the highest and the second-highest signatures was calculated. If a cell's signature difference was above the 25th quantile threshold, the highest signature was assigned as the cell identity. If a cell's signature difference was below the 25th quantile threshold, we did not define a subtype for that cell. Specifically, Tregs were defined by Foxp3 expression. mregDCs were identified by co-expression of Fscn1, Ccr7, Il4i1, with exclusion of cDC1 (Xcr1) and cDC2 (Cd209a) markers. Other immune and stromal subsets (B cells, macrophages, fibroblasts, epithelial cells) were annotated using established lineage markers.

Spatial feature and cell–cell interaction analysis

To calculate the colocalization matrix shown in Fig. 2A-B, we first divided the section into 84 domains (Supplementary Fig. 8A). Similar to a previous study [28], we identified insight neighboring cells for each pair of cell types and tested whether one cell type was more abundant in the vicinity of another cell type than expected randomly for each pair of cells. Two cells were considered adjacent if their centroids were within 30 µm distance. Then, we calculated a z-score and the related one-tailed p-value for the observed colocalization frequency in comparison to the null distribution that was established using permutation analysis of cells for each domain. Cell types were permuted 1000 times. To generate the final matrix, we corrected for multiple hypotheses using the Benjamini–Hochberg method.

To compare the spatial proximity of different cell types to Tregs (Fig. 2C, Supplementary 8E), the minimum Euclidean distance from each cell to its nearest Treg was calculated based on cell centroid coordinates. These minimum distances were then used to summarize the spatial relationship between Tregs and other cell types. Cell types were ranked according to the median of the minimum distances.

Specificity-corrected spatial enrichment score

To account for global spatial abundance effects (e.g., cell types that are ubiquitously distributed or form large contiguous regions) in Figs. 2D and 5A, we computed a *specificity-corrected spatial enrichment score* for each pair of cell types using the colocalization matrix shown in Fig. 2B.

For each index cell type A and each potential neighbor type B, we first obtained:

https://doi.org/10.1186/s12964-026-03304-1

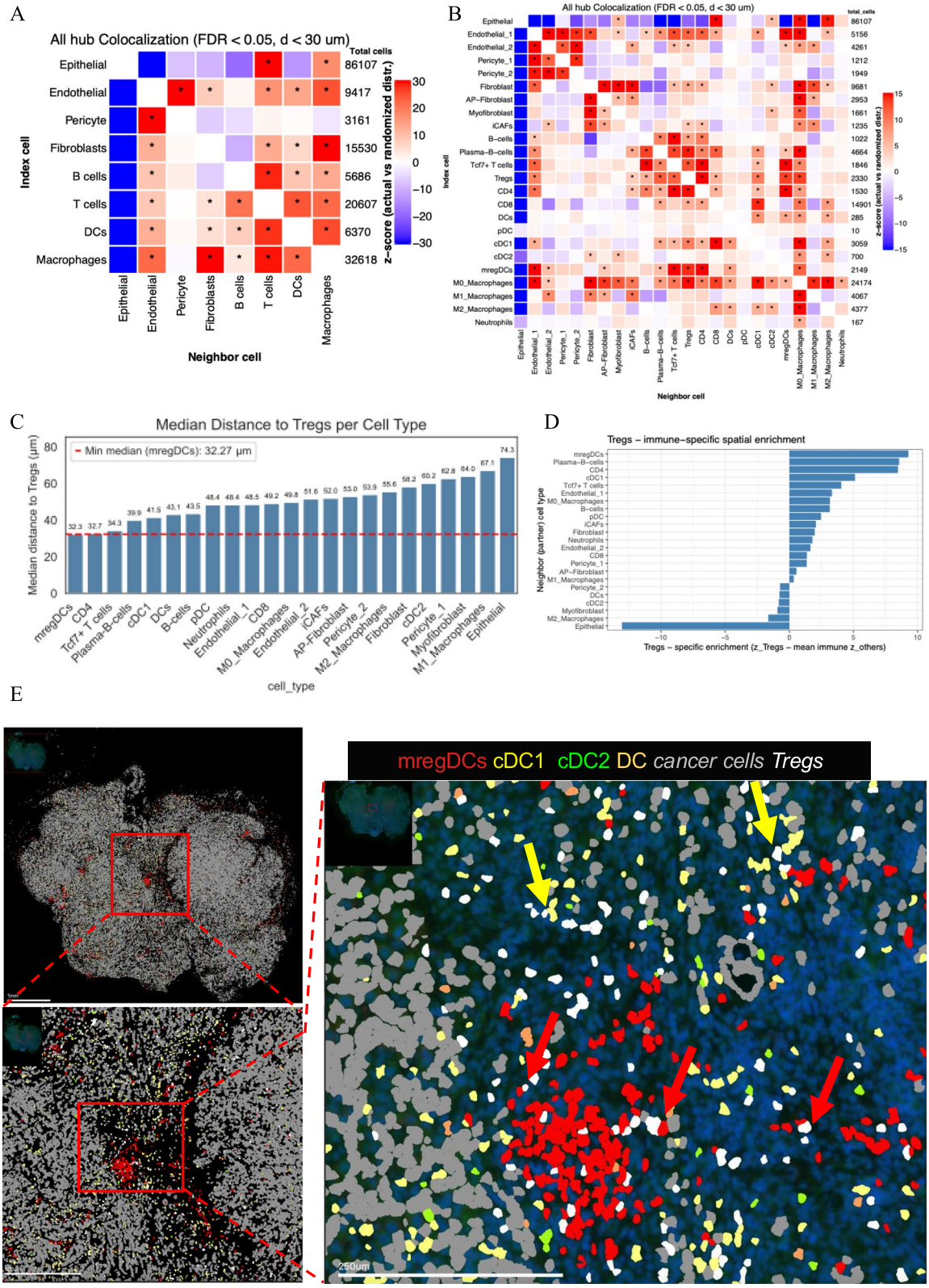


Fig. 2 Regulatory T cells co-localize with dendritic cells. **A** Colocalization analysis of cell types in the spatial transcriptomics dataset. Cells were considered neighboring if there were no other cells between them and the distance was less than 30 µm ("Methods"). High Z score indicates enriched proximity. One-tailed P-values were calculated from the mean z-score, and FDR < 0.05 (Benjamini-Hochberg) is marked with an asterisk. **B** Similar to **A**, but including all the subpopulations of cells. **C** Median spatial distance of each cell type to Tregs. Bar plot showing the median distance from each cell type to the nearest Tregs within the spatial dataset. mregDCs have the shortest median distance to Tregs (32.27 µm). **D** Specificity-Corrected Spatial Enrichment Score. The score in each bar is calculated from the colocalization matrix shown in (**B**). For each cell type, we first calculate the average Z-score values in its corresponding column and then divide the Treg Z-score by this average (see Methods). **E** Spatial localization of dendritic-cell subsets and Tregs within the tumor microenvironment. MERFISH spatial sections showing the distribution of mregDCs, cDC1, cDC2, Tregs, and malignant epithelial cells. Whole-section upper left, scale bar is 1 mm; bottom left, scale bar is 500 µm. The region indicated in the upper-left image is shown at higher magnification below. The square marks the approximate area and does not reflect the exact boundaries. High-resolution image on the right; the scale bar is 250 µm. Red arrows point to selected pairs of Tregs and mregDCs, and yellow arrows point to selected pairs of cDC1s and Tregs

1. z_A(B)—the spatial enrichment Z-score for interactions between A (as the index type) and B (as the neighbor type), derived from the permutation-based analysis. This measures how frequently cells of type B occur among the spatial neighbors of A compared to randomized label shuffles.
2. z_mean_others(B)—the mean Z-score for B computed across all other index immune cell types (i.e., all immune cell types except A). This captures the *background tendency* of B to appear near any immune cell type, reflecting its global abundance and spatial autocorrelation.

We then defined the specificity-corrected enrichment for A interacting with B as:

$$z_specific(A,B) = z_A(B) - z_mean_others(B).$$

A positive z_specific(A,B) indicates that B is enriched near A more strongly than it is near other cell types, corresponding to an A-specific spatial niche.

Values near zero indicate that A-B enrichment is not stronger than the general background enrichment of B across all cell types (e.g., when B is highly abundant or broadly distributed). Negative values indicate that B is found near A less than expected based on its interactions with other cell types.

Single-cell RNAseq data processing and analysis

We utilize a tailored pipeline similar to the one used for spatial analysis to identify cell types and states in the scRNA-seq experiment. Single-cell gene expression datasets were analyzed using the Scanpy library. Doublet detection was executed employing Scrublet with default settings, and cells exceeding a doublet score of 0.36 were filtered out. Cells with counts mapped to fewer than 200 genes and those with mitochondrial gene content exceeding 10% were excluded. Additionally, genes detected in fewer than three cells were removed. Total gene UMI per cell was normalized to a target sum of 10^4 and subjected to a log1p transformation. Subsequently, highly variable features were identified based on a minimum and maximum mean expression of 0.0125 and 3, respectively, and a minimum dispersion of 0.5. PCA was utilized for dimensionality reduction, and 50 principal components were employed for constructing a neighborhood graph with default parameters. The Leiden algorithm was employed for clustering across resolutions ranging from 0.4 to 0.8. The dataset was visualized in two dimensions using UMAP. For in-depth analysis of significant cell types (Tregs, mregDCs, and macrophages), the initial dataset was subset and re-clustered following the abovementioned methodology. Clusters were annotated using canonical markers. Differential gene expression analysis was conducted using Seurat's FindMarkers function via the Wilcoxon test, leveraging the log-transformed expression matrix.

To infer cell–cell communication, ligand–receptor inference was conducted by integrating expression and spatial adjacency matrices using LIANA [29] and NicheNet [30] frameworks. For each interacting cell pair (e.g., Treg–mregDC), ligand–receptor scores were computed as the product of normalized expression and

spatial proximity weights, allowing identification of enriched signaling axes (e.g., Ifng–Ifngr1/Ifngr2, Tngsf11–Tngrsf11a/Tngrsf11b, Il15-Il2ra/Il2rb).

Bulk RNA-seq

Total RNA was extracted from BMDCs treated with Treg supernatant using the Quick-RNA Miniprep Kit, following the manufacturer's instructions. RNA quantity and integrity were assessed by Qubit and Bioanalyzer (Agilent), and only samples with an integrity number (RIN)≥9 were processed. Poly(A)+mRNA was enriched with KAPA Pure Beads, and strand-specific libraries were prepared using the KAPA Stranded mRNA-Seq Kit according to the recommended protocol with 12 PCR cycles. Libraries were pooled equimolarly and sequenced on an Illumina Nova-seq.

Analysis of published human PDAC spatial transcriptomic and scRNA-seq data

Published spatial transcriptomic and matched single-cell RNA-seq data from patients with PDAC were obtained from Chen et al. [31]. Spatial transcriptomic data were analyzed using Scanpy. 14 patient samples with more than 2,000 spots were included. Gene expression values were normalized to a total of 10,000 counts per spot and log-transformed before downstream analysis.

Treg, mregDC and CD8 signature scores were calculated for each spatial spot using Scanpy's score_genes function. The Treg signature included FOXP3, IL2RA, CTLA4, TIGIT, and IKZF2, the mregDC signature included FLT3, CCR7, LAMP3, CCL19, FSCN1, and CD274 and the CD8 T cells signature included CD8A and CD8B. Within each patient, spots with scores above the 80th percentile were defined as Treg-high, mregDC-high or CD8 T cells high.

The enrichment of mregDC–Treg co-occurrence relative to mregDC–$CD8^+$ T-cell co-occurrence was calculated independently for each patient. First, separate odds ratios (OR) were calculated for mregDC–Treg co-occurrence and for mregDC–$CD8^+$ T-cell co-occurrence. Then, the log ratio of ORs was calculated as log(OR(mregDC-Treg)/(OR(mregDC-$CD8^+$)). Positive values therefore indicated a stronger Treg– mregDC than mregDC–$CD8^+$ T-cell association. The delta method was used to calculate the sampling variance of the log ratio of ORs. Patient-specific log ratios of ORs were combined using a random-effects model. The pooled estimate was exponentiated and represented in a forest plot as the ratio of ORs with a 95% confidence interval. Analyses were performed in R using the metafor package.

To assess the functional states associated with these spatial groups, gene-program scores were calculated for $CD8^+$ T-cell exhaustion, Treg suppressive activity, and immune-checkpoint signaling. The $CD8^+$ T-cell exhaustion signature included PDCD1, LAG3, HAVCR2, TOX, ENTPD1, and CD8. The Treg suppressive signature included FOXP3, IL2RA, CTLA4, TIGIT, IKZF2, ENTPD1, and NT5E. The immune-checkpoint signature included CD274, PDCD1LG2, PDCD1, CTLA4, LAG3, HAVCR2, and TIGIT.

For each gene program, we tested whether the mregDC–Treg spots had a higher score than both the Treg spots and the mregDC spots. At the patient level, one-sided paired Wilcoxon signed-rank tests were performed for mregDC–Treg spots vs mregDC spots and for mregDC–Treg spots vs Treg spots. The resulting p-values were corrected for multiple comparisons using the Benjamini–Hochberg method. Next, for each gene program, patient-level median differences were calculated between mregDC–Treg spots and Treg spots, and between mregDC–Treg spots and mregDC spots. These were represented as 2 vectors, and a one-sided Wilcoxon signed-rank test was used to calculate a set of 2 aggregated p-values for each gene program. Those p-values were combined by the intersection–union approach and adjusted by the Benjamini–Hochberg method, resulting in one FDR for each gene program.

The matched scRNA-seq dataset was analyzed on http://pdac.cancer-pku.cn/. Expression of selected Treg and DC-associated genes was compared across Tregs, pDCs, cDC1s, cDC2s, and mregDCs.

Statistical analysis

All statistical analyses were performed in Python 3.9 or R 4.4. Comparisons between groups were made using unpaired t-test unless otherwise stated. Spatial enrichment p-values were derived from permutation-based z-scores using one-tailed normal approximation, and results with adjusted $p < 0.05$ were considered significant.

Software

Throughout the paper, we report analysis performed using Python (v 3.9.18), R (v 4.4.3), numpy (v 1.26.4), pandas (v 2.3.1), matplotlib (v 3.9.4), seaborn (v 0.13.2), scanpy (v, 1.10.3), squidpy (v 1.5.0), Seurat (v 5.3.0), nichenetr (2.2.0), liana (0.1.14), ggplot2 (v 4.0.0), ggpubr (v 0.6.0), circlize (v 0.4.16), Complex Heatmap (v 2.20.0), scpubr (v 3.0.0), and the MERSCOPE Visualizer (v 2.5) by Vizgen.

A detailed list of plasmids, oligos, and reagents is listed in the supplementary data section.

Results

Tregs interact with dendritic cells in PDAC TME

To explore the interactions between immune cells and other cell types in PDAC tumors, we used 6499c4 pancreatic cancer cells [25] derived from tumors developed in a genetically engineered mouse model and injected them into the pancreas of syngeneic C57BL/6 mice. Twelve days after cell injection, we recovered the tumors and performed scRNA-seq and spatial transcriptomics (Fig. 1A). For the scRNA-seq experiment, half of the tumor was dissociated [26], and the analysis allowed the identification of multiple cell types (Fig. 1B-C) and subtypes, including epithelial malignant cells, fibroblasts, T cells, endothelial cells, macrophages, and dendritic cells (Supplementary Figs. 1-4). We have used this analysis, in conjunction with our previous studies and publications [5, 32], to define a set of 183 genes that included 3–4 representative genes for each cell subpopulation.

The remaining half of the tumor was formalin-fixed, and successive sections were subjected to H&E staining and spatial transcriptomics (Fig. 1D–E) via MERFISH technology [33]. We have analyzed 179,496 cells in the section, detecting an average of 418 transcripts per cell. We identified three major hubs enriched in either cancer epithelial cells, stromal cells, or immune cells (Fig. 1E). We then examined the identity of each cell type and subtype in the spatial transcriptomic data (Fig. 1F-H, Supplementary Figs. 1B, 1D), including fibroblasts, T cells (Supplementary Fig. 5), and myeloid cells, which could be further classified into M1 macrophages (Folr2-positive), M2 macrophages (CD274-positive), or M0 macrophages defined based on the lack of M1/M2 markers (Supplementary Fig. 6). We also identified dendritic cell subtypes, including pDCs, cDC1, cDC2, and mregDCs (Supplementary Fig. 7).

To assess the spatial proximity between different cell types, which reflects potential cell–cell interactions, we performed neighboring cell analysis (see "Methods" [28, 32]). The section was divided into 83 domains (Supplementary Figs. 8A–B), and neighboring analyses were conducted to identify significant associations between cell subtypes (Fig. 2A-B).

As expected, cancer cells predominantly interacted with each other within cancer-dense regions, while immune and stromal cells were colocalized (Figs. 1E and 2A; Supplementary Fig. 8C). M1 macrophages were mostly excluded from the tumor core, whereas other macrophage populations infiltrated the tumor mass (Supplementary Fig. 8D). Interestingly, Tregs were found in proximity to DCs—particularly mregDCs and cDC1 (Fig. 2C-D; Supplementary Fig. 8E). Notably, mregDCs formed clusters, whereas other immune cell types were dispersed throughout the stromal and immune domains (Fig. 2E).

To assess the reproducibility of these findings, we analyzed an independent orthotopic PDAC model generated using a cell line derived from tumors arising in Ptf1a-CreER; $Trp53^{fl/fl}$; LSL-$Kras^{G12D}$ mice (Supplementary

https://doi.org/10.1186/s12964-026-03304-1

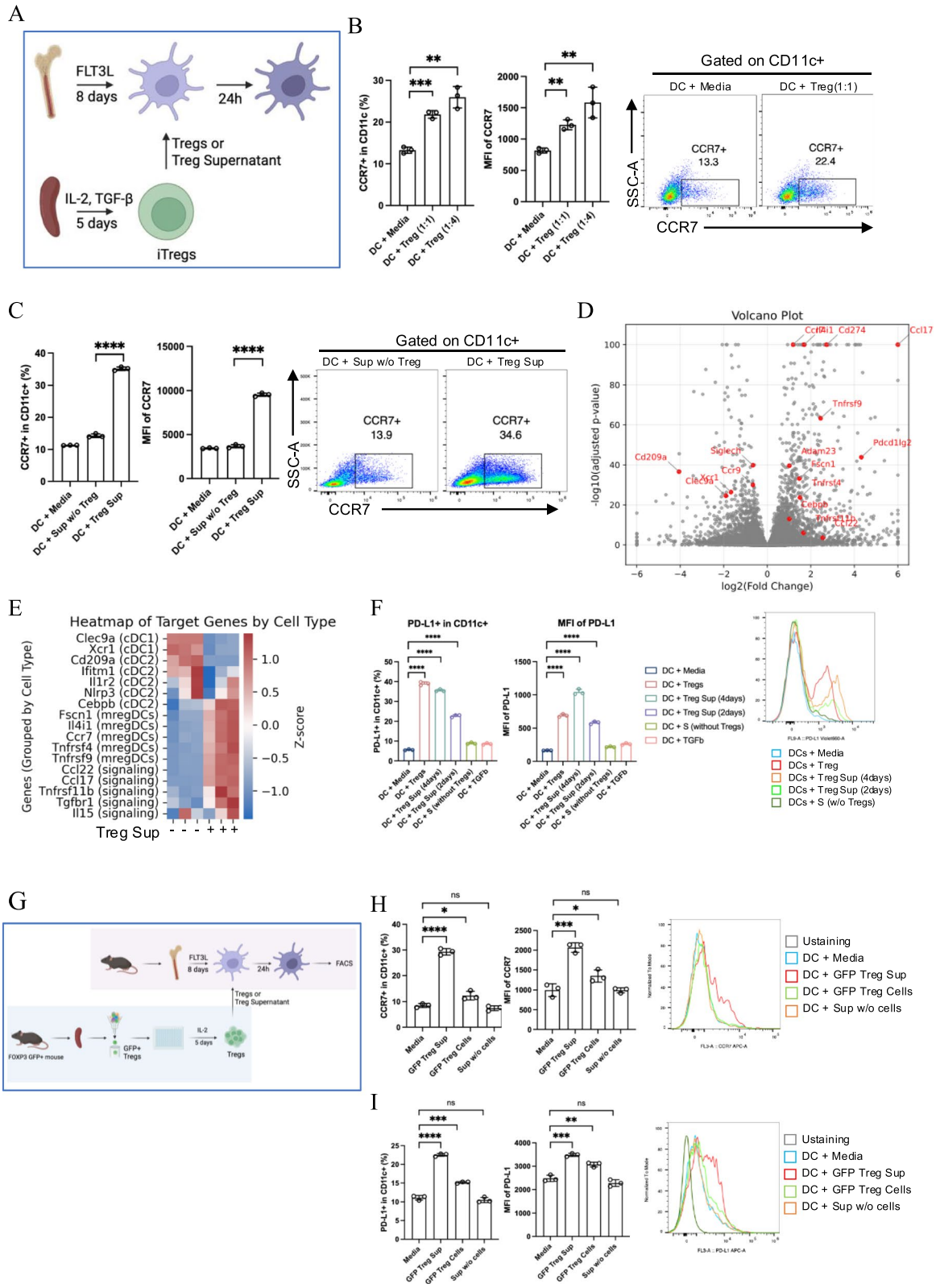


Fig. 3 Tregs' supernatant induces the transition from conventional dendritic cells to mregDCs. **A** An overview of the procedure to test the effect of Treg and dendritic cell interactions. **B** Quantification of Flow cytometry analysis showing the levels of CCR7 expression in FLT3L-differentiated BMDCs after incubation with different ratios of iTregs, media was used as a control. Percentages of CCR7-positive DCs on the left and CCR7 mean fluorescence intensity (MFI) (middle). Representative flow cytometry plots are on the right. The figure includes three technical replicates, and the experiment was repeated three times, showing similar results. **C** FLT3L-differentiated BMDCs were treated with Treg supernatant after culture for five days with media or with control media that include IL-2 and TGF-β1 (Sup w/o Treg). Percentages of CCR7-positive DCs on the left and CCR7 mean fluorescence intensity (MFI) (middle). Representative flow cytometry plots are on the right. The figure includes three technical replicates, and the experiment was repeated three, showing similar results. **D** Volcano plot showing enriched genes in FLT3L-differentiated BMDCs exposed to Treg supernatant (Right) versus control media (Left), based on bulk RNA-seq experiment. Selected differentially expressed genes are highlighted. **E** Heatmap showing expression of selected genes based on the RNA-seq data shown in (**E**). Gene-wise z-score normalization was applied to the expression matrix. **F** FLT3L-differentiated BMDCs were treated with Treg supernatant or with control media as indicated. Percentage of PD-L1-positive DCs is shown on the left, and PD-L1 mean fluorescence intensity (MFI) is shown in the middle. Representative flow cytometry plots are on the right. The figure includes three technical replicates, and the experiment was repeated four times, showing similar results. **G** Overview of experiments using native FOXP3$^+$ Tregs to validate Treg-induced DC reprogramming. Splenic FOXP3-GFP$^+$ Tregs were sorted and co-cultured with FLT3L-differentiated BMDCs. Alternatively, we used the FOXP3-GFP$^+$ Treg supernatant, media without cells (media), or media with cytokine (sup without cells). **H-I** BMDCs were analyzed for CCR7 (**H**) and PD-L1 (**I**) induction to assess whether native Tregs recapitulated the effects observed with in vitro-generated iTregs. The figure includes three technical replicates, and the experiment was repeated three times, showing similar results. Statistical significance was determined using an unpaired two-tailed Student's t-test. Data represent mean ± SD. * $p<0.05$; ** $p<0.01$; *** $p<0.001$; **** $p<0.0001$

Fig. 9). A similar pattern of interactions between T-cell subsets and DC subpopulations was observed in this model.

Together, these spatial transcriptomic analyses reveal a close interaction between Tregs and DCs subpopulations within the PDAC TME.

Tregs induce cDC differentiation to mregDCs

To investigate the effect of the interactions between DCs and Tregs, we generated Tregs and DCs in vitro. We recovered bone marrow cells and differentiated them into DCs using FLT3L [34, 35]. In parallel, we recovered splenic CD4 T cells and added TGF-β1 and IL2 to generate inducible Tregs (Supplementary Fig. 10A-B). Co-incubation of bone marrow-derived cells (BMDCs) and Tregs (Fig. 3A) induced the expression of CCR7 in DCs (Fig. 3B). To test if the effect was mediated by physical interaction or secreted molecules, we repeated the experiment using Treg supernatant or, as a control, we included only the cytokines that are used to differentiate CD4 T cells into Tregs. Treg supernatant induced the expression of CCR7, while the media that included only TGF-β1 and IL2 did not affect CCR7 expression (Fig. 3C; Supplementary Fig. 10C). This finding raises the possibility that Tregs secreted molecules induce the differentiation of conventional DCs toward mregDCs. To examine this possibility, we added Treg supernatant to BMDCs and performed bulk RNA-seq. We found that the expression of cDC1 and cDC2 markers was reduced, and the expression of CCR7, as well as other mregDC markers, such as Fscn1, increased (Fig. 3D-E). Consistently, we have also detected an increase in the expression of PD-L1 under the same conditions, suggesting a potential immunosuppressive effect of the same cells (Fig. 3F; Supplementary Fig. 10D-F). We repeated the experiment using native Tregs that were isolated from mice (FOXP3-GFP) and found a similar effect, supporting the possibility that the same molecules are expressed by Tregs in vivo (Fig. 3G-I). Interestingly, Tregs did not affect the expression of CCR7 in BMDCs that were differentiated with GM-CSF (Supplementary Figs. 10G-H). Previous studies question the similarity of GM-CSF-differentiated bone marrow (BM) cells to DCs, suggesting that some of these cells are more similar to macrophages [36]. The effect of Treg supernatant on FLT3L BM-differentiated cells but not on GM-CSF BM-differentiated cells, supports the possibility that the described interactions and effect of Tregs are specific for DCs.

https://doi.org/10.1186/s12964-026-03304-1

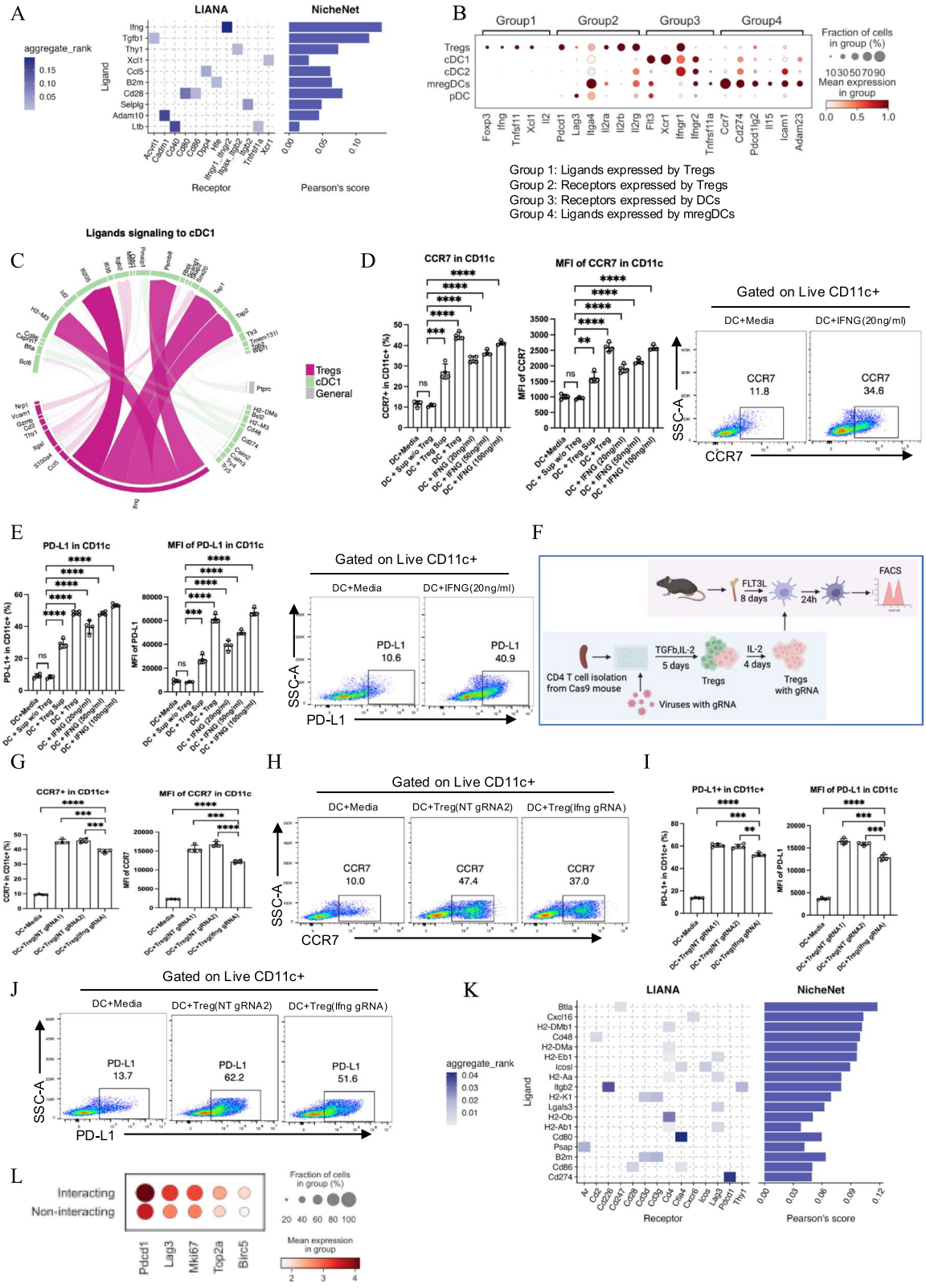


Fig. 4 Bidirectional interactions between cDCs and Tregs. **A** Ligand–receptor interaction analysis between Tregs and cDC1s using the scRNA-seq data. LIANA tool results are presented on the left, and the heatmap summarizes the ligand-receptor interaction scores between Treg-derived ligands and cDC1-expressed receptors. Lower scores indicate stronger predicted interaction. The ranking plot on the right displays the top ligand activities prioritized by Nichenet, highlighting ligand candidates most likely to drive transcriptional changes in cDCs. **B** Expression of selected ligand and receptor genes in Tregs and DC subsets. Dot plot showing the expression level and abundance in each subpopulation. Genes were divided into groups according to the legend at the bottom of the panel. **C** Chord diagram summarizing predicted ligand–receptor interactions between Tregs and cDC1. Ligands are expressed by Tregs, and receptors are expressed by cDC1s. Ligand–receptor interactions were inferred using the LIANA framework based on our scRNA-seq dataset. Lines represent individual ligand–receptor pairs, and line width reflects interaction scores based on the LIANA tool. **D** The percentage of $CCR7^+$ cells at different concentrations of IFN-γ, based on Flow cytometry analysis (left), The negative control group was cultured in basal media. The MFI is shown in the middle panel. Representative flow cytometry plots (right) illustrate the increase in $CCR7^+$ BMDCs following IFN-γ stimulation. **E** Similar to **D**, showing the expression level of $PD\text{-}L1^+$. The figures in **D** and **E** include three technical replicates and were repeated three times, showing similar results. **F** Overview of the CRISPR-based Treg perturbation assay used to test the effect of Treg-derived IFN-γ on BMDCs. Transduced Tregs were sorted and incubated with IL2 before co-culture with BMDCs. **G** Quantification of $CCR7^+$ $CD11c^+$ BMDCs (left) and CCR7 MFI (right) following co-culture with control Tregs or Tregs that were transduced with gRNAs targeting IFN-γ, or non-targeting gRNA (NT). The basal medium was used as a negative control to show the basal expression of CCR7. **H** Representative flow cytometry plots showing CCR7 induction in BMDCs co-cultured with CRISPR-edited Tregs. **I** Quantification of $PD\text{-}L1^+$ $CD11c^+$ BMDCs (left) and PD-L1 MFI (right) following co-culture with control Tregs or Tregs transduced with gRNAs targeting IFN-γ or a non-targeting gRNA as a control. The basal medium was used as a negative control to show the basal expression of PD-L1. **J** Flow cytometry plots illustrating PD-L1 induction in BMDCs co-cultured with CRISPR-edited Tregs. NT: Non-Target. The figures in **G** and **I** include three technical replicates and were repeated three times, showing similar results. **K** Ligand-receptor interaction analysis between cDC1 and Tregs using the scRNA-seq data. The heatmap summarizes the predicted ligand-receptor interaction scores between cDC1-derived ligands and Treg-expressed receptors. **L** Dot plot showing differential gene expression between interacting and non-interacting Tregs. Interacting Tregs are defined as cells spatially adjacent to cDC1. Dot color represents the mean expression level within each group, and dot size indicates the percentage of cells expressing each gene. Statistical significance was determined using an unpaired two-tailed Student's t-test. Data represent mean ± SD. * $p<0.05$; ** $p<0.01$; *** $p<0.001$; **** $p<0.0001$

IFN-γ mediates the induction of cDC differentiation into mregDCs

To identify cytokines and secreted molecules mediating the interactions between Tregs and cDC1s, we performed ligand–receptor analysis using the scRNA-seq dataset generated in this study (Figs. 1 and 4A). We applied the LIANA tool [29], and the analysis revealed several candidate ligand–receptor pairs, including Ifng–Ifngr and Xcl1–Xcr1. Among these, Ifng was expressed by Tregs, whereas Ifngr was expressed by cDC1s (Fig. 4B). Although Ifng is known to be expressed by Th1 and CD8 T cells, expression of Ifng by Tregs was reported before [37–40], consistent with our finding.

We next used NicheNet [30] to assess the predicted effects of these signaling interactions on cDC1 gene expression and found that Ifng exhibited the strongest predicted influence (Fig. 4C). To validate these predictions, we treated FLT3L-derived BMDCs with IFNG and observed induction of CCR7 and PD-L1 expression (Fig. 4D-E), whereas other Treg-secreted cytokines did not produce this effect (Supplementary Fig. 11E).

To further confirm the role of Ifng, we employed CRISPR/Cas9-mediated gene targeting. $CD4^+$ T cells were isolated from Cas9-expressing mice, transduced with gRNA-Ifng-mCherry. mCherry + cells were sorted and cultured for another 4 days, and then co-cultured with BMDCs. Ifng -targeted Tregs induced a markedly weaker response in BMDCs compared with control Tregs (Fig. 4F–J). Interestingly, a similar effect of IFNg on the maturation of human monocyte-derived dendritic cells (moDCs) has previously been reported [41]. Notably, Ifng-targeted Tregs still partially induce CCR7 and PD-L1 expression, suggesting that additional signals, in addition to Ifng, contribute to the induction of mregDCs. Furthermore, our data do not exclude the possibility that IFN-γ produced by other cell types also contributes to the differentiation of cDCs into mregDCs.

We also examined whether the interaction between cDC1s and Tregs reciprocally affects Treg phenotype. Using two complementary approaches—(i) LIANA [29] and NicheNet [30] analyses (Fig. 4K), and (ii) spatial transcriptomic comparison of Tregs in proximity versus distant from cDC1s (Fig. 4L)—we found that Tregs

https://doi.org/10.1186/s12964-026-03304-1

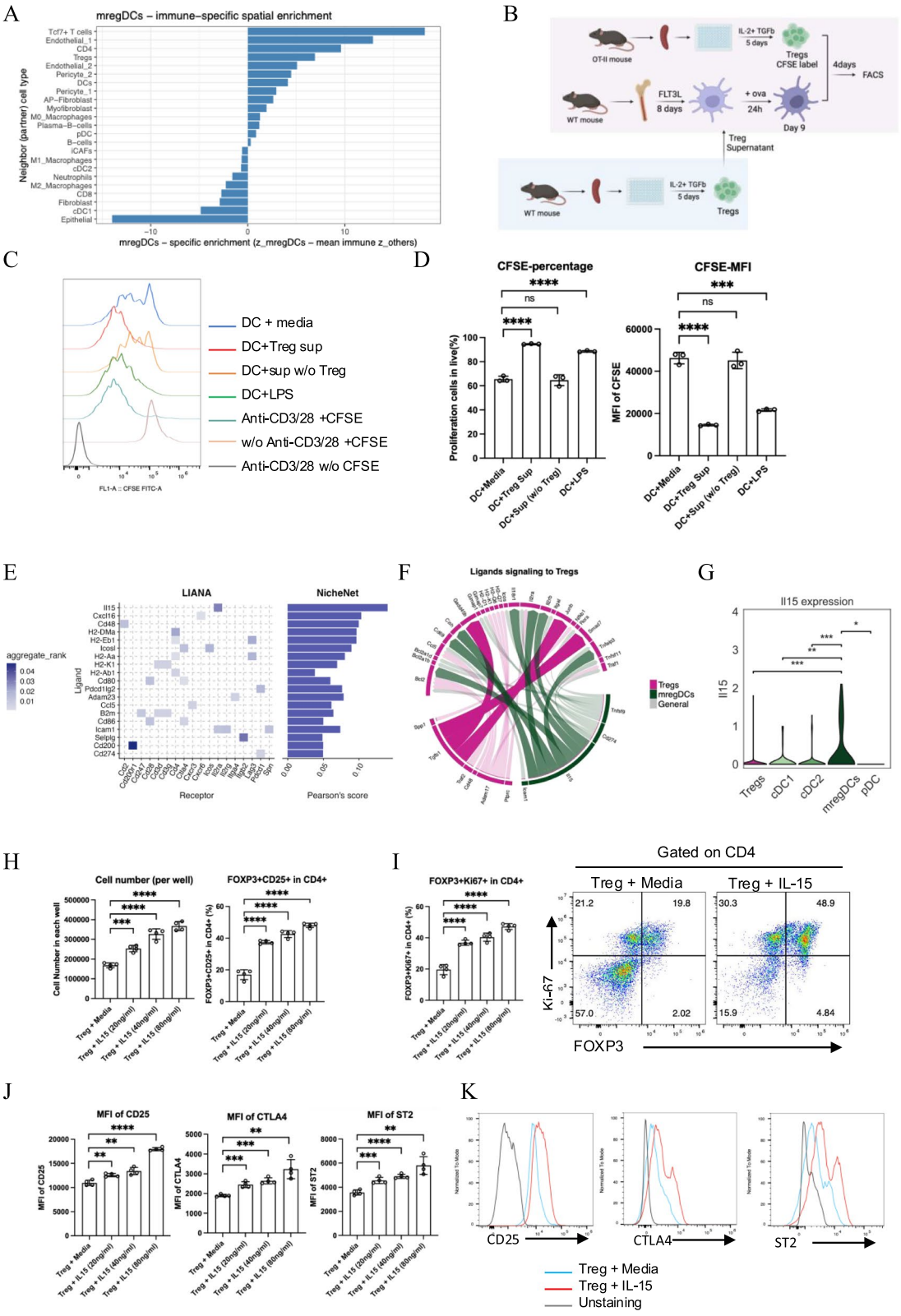


Fig. 5 mregDCs induce Treg proliferation. **A** Specificity-Corrected Spatial Enrichment Score. The score in each bar is calculated from the colocalization matrix shown in Fig. 2B. For each cell type, we first calculate the average Z-score values in its corresponding column and then divide the mregDCs Z-score by this average (see Methods). **B** An overview of the experiment that tests the effect of mregDCs on Treg gene expression and proliferation. **C** CFSE dilution profiles showing proliferation of CFSE-labeled Tregs following co-culture with BMDCs, or treated under the conditions indicated in the figure. The BMDCs were preconditioned with Treg-derived supernatant. The anti-CD3/CD28 stimulation group was used as a positive control for Treg proliferation, and LPS stimulation was used as a positive control for DC activation. Anti-CD3/CD28-stimulated Treg cells without CFSE staining were used as CFSE-negative control groups to evaluate the basal signal value of CFSE. **D** Quantification of Treg proliferation induced by BMDCs preconditioned with Treg-derived supernatant. The proportion of CFSE-positive T cells (left) and CFSE MFI (right) in the different conditions is shown. The figure includes three technical replicates, and the experiment was repeated three times, showing similar results. **E** Ligand-receptor interaction analysis between mregDCs and Tregs using the scRNA-seq dataset. The heatmap summarizes the ligand-receptor interaction scores between mregDCs-derived ligands and Treg-expressed receptors. **F** Chord diagram summarizing predicted ligand-receptor interactions between Tregs and mregDCs. Circos plot visualizing the strength and direction of ligand-receptor interactions identified by LIANA. Lines represent individual ligand–receptor pairs, and line width reflects interaction scores based on the Liana tool. **G** Violin plots show *Il15* transcript levels in Tregs, cDC1, cDC2, mregDCs, and pDCs based on the scRNA-seq data. The Y-axis represents the log-normalized expression levels of *Il15* in each cell. P-values were calculated using the Mann–Whitney U test (two-sided). Significance thresholds were set at $p<0.05$ (*), $p<0.01$ (**), and $p<0.001$ (***). **H** In vitro induced iTreg cells were treated with IL-15. On the left, the total number of Tregs after one day of culture in media alone or supplemented with increasing concentrations of recombinant IL-15. On the right, the frequency of $FOXP3^+CD25^+$ Tregs within the $CD4^+$ population under the same culture conditions. **I** On the left, the quantification of $FOXP3^+Ki\text{-}67^+$ cells within the $CD4^+$ population after one day of culture with the indicated concentrations of recombinant IL-15. On the right, representative flow cytometry plots showing FOXP3 and Ki-67 expression in $CD4^+$ T cells cultured with media alone or with IL-15. **J** MFI of CD25 (left), CTLA-4 (middle), and ST2 (right) measured in Tregs with the indicated concentrations of IL-15. **K** Representative flow cytometry histogram overlays showing IL-15-dependent upregulation of Treg activation markers. Panels I-L include four technical replicates, which were repeated three times, showing similar results. Statistical significance was determined using an unpaired two-tailed Student's t-test. Data represent the mean ± SD. * $p<0.05$; ** $p<0.01$; *** $p<0.001$; **** $p<0.0001$

interacting with cDC1s exhibited increased expression of receptors involved in immunosuppressive signaling, including PD-1 and LAG3.

In summary, these results indicate that Treg-secreted IFN-γ drives the differentiation of cDC1s into mregDCs, while cDC1s, in turn, promote a more immunosuppressive Treg phenotype.

MregDCs are the closest neighbors of Tregs and may promote their proliferation through IL15

We found that MregDCs were the nearest neighboring cells to Tregs (Fig. 2C-D and Supplementary 11B-C), and Tregs are closer to mregDCs than CD8 T cells (Fig. 5A). To test the functional consequences of these predicted interactions, we treated FLT3L-derived BMDCs with Treg supernatant to induce an mregDC-like state and subsequently incubated them with OVA peptide and differentiated Tregs (Fig. 5B). We found that the interaction with mregDCs enhanced Treg proliferation (Fig. 5C-D).

Next, we sought to identify the molecules mediating this effect using Liana [29] and NicheNet [30] analyses (Fig. 5E–F). These analyses predicted that IL15, which is mainly expressed by mregDCs in mouse models and human PDAC (Fig. 5E-G, Supplementary 12), influences Treg gene expression. To test this prediction, we incubated differentiated Tregs with recombinant IL15 (Supplementary 11A) and observed that IL15 upregulated the proliferation marker Ki67 (Fig. 5H-I) as well as genes associated with Treg activation and immunosuppressive function, including CD25, CTLA4, and ST2 (Fig. 5J-K).

Next, we profiled the ligand-receptor interactions to test the possible effect of Tregs on mregDCs (Supplementary 11D-E). TNFSF11 (RANKL) was identified as a cytokine that is expressed by Tregs, and TNFRSF11A was expressed by mregDCs but not by other DC subtypes (Supplementary 11F). To test if TNFSF11 affects mregDCs, we differentiated BM cells with FLT3L and treated the cells with LPS to induce a cell state that is similar to mregDCs. We then added recombinant TNFSF11 and found that the expression of CCR7 was further elevated (Supplementary 11G-H). To further validate the role of Tnfsf11, we transduced lentivirus encoding

gRNA-Tnfsf11-mCherry into $CD4^+$ T cells. mCherry + cells were selected and cultured for 4 days before being co-cultured with BMDCs. Compared to control Treg cells, the response induced by Tnfsf11-targeted Treg cells was significantly weakened (Supplementary 11I-J).

Together, these findings indicate that interactions between mregDCs and Tregs increase Treg abundance within the TME and enhance their immunosuppressive phenotype, and that IL15 possibly serves as a key mediator of this effect. The Tregs can also affect mregDCs, increasing the expression of their migratory receptors.

MregDCs and Tregs co-localize in human PDAC

To determine whether the spatial association between mregDCs and Tregs observed in mouse tumors is also present in human PDAC, we reanalyzed published spatial transcriptomic data from 14 patients with PDAC (Chen et al., [31]). We identified spots enriched for mregDC or Treg signatures, as well as spots enriched for both signatures (Supplementary Fig. 12A–C). Across 14 patients, the frequency of spots containing both mregDC and Treg signatures was higher than expected based on the abundance of spots containing either signature alone ($p < 0.001$ Fisher's exact test; Supplementary Fig. 12D). These findings indicate that mregDCs and Tregs preferentially co-localize in human PDAC, consistent with our observations in mouse tumors.

Reanalysis of scRNA-seq data from the same patients further showed that mregDCs express IL15 (Supplementary Fig. 12E). We next examined transcriptional programs associated with spatial regions enriched for mregDCs, Tregs, or both cell populations. Spots enriched for both mregDC and Treg signatures showed significant enrichment of gene programs associated with $CD8^+$ T-cell exhaustion (FDR < 0.01), and Treg suppressive activity (FDR < 0.01), in most patients, suggesting that the spatial association between mregDCs and Tregs is linked to an immunoregulatory state within the tumor microenvironment (Supplementary Fig. 12F).

Finally, we compared the spatial enrichment of mregDC–Treg and mregDC–$CD8^+$ T-cell co-occurrence. In 11 of 14 patients, mregDC–Treg co-occurrence was more abundant than mregDC–$CD8^+$ T-cell co-occurrence (one-sided $P = 0.021$), indicating a preferential spatial association between mregDCs and Tregs in human PDAC (Supplementary Fig. 12G).

Together, these analyses demonstrate that the preferential spatial association between mregDCs and Tregs observed in our mouse models is also present in human PDAC and is associated with transcriptional programs indicative of related function.

Discussion

The number of dendritic cells (DCs) present in the TME has a major impact on antitumor immunity [42]. In pancreatic cancer, DC abundance is particularly low, and increasing DC numbers using FLT3L together with ICIs can improve antitumor responses and restrict tumor growth in animal models [22, 23]. However, DC colocalization in the TME is also an important factor that can affect the overall immune response. DCs can interact with Tregs and with $CD8^+$ T cells, and these interactions are predicted to exert opposing effects on the immune response [15–17, 19, 20, 43, 44]. Thus, the relative spatial proximity among DCs, Tregs, and $CD8^+$ T cells is critical. Moreover, distinct T-cell subsets engaging with specific DC subsets may yield different outcomes, ultimately shaping the overall immune competence within the tumor.

Here, we used spatial transcriptomics to rank DC–T-cell interactions in situ (Fig. 2), showing that Tregs are closer to DCs than to CD8 T cells (Figs. 2 and 5). We integrated these findings with ligand–receptor analysis of scRNA-seq, followed by in vitro validation. We show that cDC1 cells interact with Tregs, and that this interaction induces Treg activation and upregulation of immunosuppressive genes such as *Lag3* and *Pdcd1* (Fig. 4). This effect is bidirectional, as cytokines secreted by Tregs promote the transition of cDC1 into the mregDC state (Fig. 3). Thus, despite prior studies suggesting that Tregs limit DC maturation [10, 16, 45, 46] or co-stimulatory

molecule expression, our in vitro experiments indicate that Treg-derived cytokines can enhance the transition of cDC1 into mregDCs.

The mregDCs, in turn, support Treg proliferation and enhance their immunosuppressive phenotype. Our data suggest that IL-15 expressed by mregDCs may promote Treg expansion and induce expression of inhibitory receptors such as CTLA-4 (Fig. 5). Thus, in vivo spatial organization combined with in vitro assays suggests that reciprocal interactions between Tregs and DCs create a reinforcing feedback loop that may support the establishment of an immunosuppressive TME (Supplementary Fig. 13).

It is still not clear why mature CCR7-positive DCs do not migrate to the lymph node and what is the molecular mechanism that traps them in the tumor, but our study shows the possible benefit to the tumor by supporting the expansion of Tregs. As a consequence, therapeutic strategies aimed at increasing DC numbers may need to be paired with interventions that disrupt the Treg–DC circuit. Our analyses highlight IFNG, IL15, and TNFSF11 as key mediators of these multicellular interactions. Consistent with our findings, IFNG has been implicated in promoting Treg-related responses together with additional factors [40]; however, targeting it, is challenging, given its essential role in $CD8^+$ T-cell and NK-cell activation and cytotoxicity. Still, targeting TNFSF11 and IL-15 may weaken this positive feedback loop and reduce immunosuppression with minimal unwanted effects on protective anti-tumor immunity.

In summary, despite the dual potential functions of mregDCs as mature and suppressive DCs, the data presented here suggest that Tregs promote the mregDC state, and mregDCs, in turn, enhance Treg activation and proliferation. Thus, the proximity between the cells supports the immunosuppressive outcome. A deeper understanding of DC function in the PDAC TME has clinical relevance, particularly in light of encouraging early results of pancreatic cancer vaccine clinical trials [47, 48], which previously were shown to be mediated by DCs [49].

Supplementary Information The online version contains supplementary material available at https://doi.org/10.1186/s12964-026-03304-1.

Acknowledgements We thank all members of the Parnas laboratory for their encouragement and ideas. We thank Idit Shiff and Abdelmajeed Nasereddin for scRNA-seq library preparation. We thank Dr. Yi Sun, Dr. Cheng-Yi Chen and Jiang He from Vizgen Lab Services for sample processing and MERFISH results. All the cartoons were created with BioRender.com. This project received funding from the Israel Cancer Research Fund (Acceleration Grant), Hirshberg Foundation seed grant, Israel Cancer Association grant number 20240118, Israel Science Foundation grant (No. 3614/24), the Alex U. Soyka Program, US-Israel Binational Science Foundation (BSF) application 2021329 and 2023314, MOST-CYPRUS PROJECT CYPHRUS 0007595.

Authors' contributions O.P and Y.H designed the study and wrote the manuscript. Y.H made the experiments with help from S.T-B. O. Y-L performed the spatial transcriptomic and scRNA-seq experiments under the mentorship of J.C. M.B and V.H. provided the FOXP3 mice and sorter FOXP3-GFP cells. Y.H performed the computational analysis with help from S.A-B, Y.S, and A. S-P. Y.S, Y.H, H.B.K and W.L.H performed and support the analysis of human data.

Funding This project received funding from the Israel Cancer Research Fund (Acceleration Grant), Hirshberg Foundation seed grant, Israel Cancer Association grant number 20240118, Israel Science Foundation grant (No. 3614/24), the Alex U. Soyka Program, US-Israel Binational Science Foundation (BSF) application 2021329 and 2023314.

Data availability Data was deposited in GEO, bulk RNA-seq GSE314740, single cell RNA-seq GSE314742 and spatial transcriptomic data GSE314806.

Declarations

Competing interests The authors declare no competing interests.

Open Access This article is licensed under a Creative Commons Attribution-NonCommercial-NoDerivatives 4.0 International License, which permits any non-commercial use, sharing, distribution and reproduction in any medium or format, as long as you give appropriate credit to the original author(s) and the source, provide a link to the Creative Commons licence,

and indicate if you modified the licensed material. You do not have permission under this licence to share adapted material derived from this article or parts of it. The images or other third party material in this article are included in the article's Creative Commons licence, unless indicated otherwise in a credit line to the material. If material is not included in the article's Creative Commons licence and your intended use is not permitted by statutory regulation or exceeds the permitted use, you will need to obtain permission directly from the copyright holder. To view a copy of this licence, visit http://creativecommons.org/licenses/by-nc-nd/4.0/.

References

1. Siegel RL, Miller KD, Wagle NS, Jemal A. Cancer statistics, 2023. CA Cancer J Clin. 2023;73:17–48.
2. Siegel RL, Kratzer TB, Wagle NS, Sung H, Jemal A. Cancer statistics, 2026. CA Cancer J Clin. 2026;76:e70043.
3. Yachida S, et al. Distant metastasis occurs late during the genetic evolution of pancreatic cancer. Nature. 2010;467:1114–7.
4. Hruban RH, Maitra A, Goggins M. Update on pancreatic intraepithelial neoplasia. Int J Clin Exp Pathol. 2008;1:306–16.
5. Schlesinger Y, et al. Single-cell transcriptomes of pancreatic preinvasive lesions and cancer reveal acinar metaplastic cells' heterogeneity. Nat Commun. 2020;11:4516–8.
6. Amaral MJ, et al. Tumor Stroma Area and Other Prognostic Factors in Pancreatic Ductal Adenocarcinoma Patients Submitted to Surgery. Diagnostics (Basel). 2023;13:655.
7. Torphy RJ, et al. Stromal Content Is Correlated With Tissue Site, Contrast Retention, and Survival in Pancreatic Adenocarcinoma. JCO Precis Oncol. 2018;2018.
8. Brunkow ME, et al. Disruption of a new forkhead/winged-helix protein, scurfin, results in the fatal lymphoproliferative disorder of the scurfy mouse. Nat Genet. 2001;27:68–73.
9. Sakaguchi S, Sakaguchi N, Asano M, Itoh M, Toda M. Immunologic self-tolerance maintained by activated T cells expressing IL-2 receptor alpha-chains (CD25). Breakdown of a single mechanism of self-tolerance causes various autoimmune diseases. J Immunol. 1995;155:1151–64.
10. Jang J-E, et al. Crosstalk between regulatory T cells and tumor-associated dendritic cells negates anti-tumor immunity in pancreatic cancer. Cell Rep. 2017;20:558–71.
11. Zhang Y, et al. Regulatory T-cell depletion alters the tumor microenvironment and accelerates pancreatic carcinogenesis. Cancer Discov. 2020;10:422–39.
12. Kamphorst AO, et al. Rescue of exhausted CD8 T cells by PD-1-targeted therapies is CD28-dependent. Science. 2017;355:1423–7.
13. Silva Barcelos EC, Ricciuti D, Mondanelli G, Gargaro M. Rewriting the dendritic cell code in cancer-from subset identity to immunotherapeutic design. FEBS Lett. 2025;599:2060–83.
14. Moon CY, et al. Dendritic cell maturation in cancer. Nat Rev Cancer. 2025;25:225–48.
15. Moreno Ayala MA, et al. CXCR3 expression in regulatory T cells drives interactions with type I dendritic cells in tumors to restrict CD8+ T cell antitumor immunity. Immunity. 2023;56:1613-1630.e5.
16. Marangoni F, et al. Expansion of tumor-associated Treg cells upon disruption of a CTLA-4-dependent feedback loop. Cell. 2021;184:3998-4015.e19.
17. You S, et al. Lymphatic-localized Treg-mregDC crosstalk limits antigen trafficking and restrains anti-tumor immunity. Cancer Cell. 2024;42:1415-1433.e12.
18. Yang J, et al. Mature and migratory dendritic cells promote immune infiltration and response to anti-PD-1 checkpoint blockade in metastatic melanoma. Nat Comms. 2025;16:8151.
19. Maier B, et al. A conserved dendritic-cell regulatory program limits antitumour immunity. Nature. 2020;580:257–62.
20. Magen A, et al. Intratumoral dendritic cell-CD4+ T helper cell niches enable CD8+ T cell differentiation following PD-1 blockade in hepatocellular carcinoma. Nat Med. 2023;29:1389–99.
21. Lee CYC, et al. Tumour-retained activated CCR7+ dendritic cells are heterogeneous and regulate local anti-tumour cytolytic activity. Nat Commun. 2024;15:682.
22. Hegde S, et al. Dendritic cell paucity leads to dysfunctional immune surveillance in pancreatic cancer. Cancer Cell. 2020;37:289-307.e9.
23. Hogg GD, et al. Combined Flt3L and CD40 agonism restores dendritic cell-driven T cell immunity in pancreatic cancer. Sci Immunol. 2025;10:eadp3978.
24. Xia L, et al. Systematic identification of gene combinations to target in innate immune cells to enhance T cell activation. Nat Commun. 2023;14:6295–319.
25. Li J, et al. Tumor cell-intrinsic factors underlie heterogeneity of immune cell infiltration and response to immunotherapy. Immunity. 2018;49:178-193.e7.
26. Yosefov-Levi O, Tornovsky S, Parnas O. Pancreatic Tissue Dissection to Isolate Viable Single Cells. J Vis Exp. 2023:e64871. https://doi.org/10.3791/64871.

27. Andreatta M, Carmona SJ. UCell: robust and scalable single-cell gene signature scoring. Comput Struct Biotechnol J. 2021;19:3796–8.
28. Chen JH, et al. Human lung cancer harbors spatially organized stem-immunity hubs associated with response to immunotherapy. Nat Immunol. 2024;25:644–58.
29. Dimitrov D, et al. Comparison of methods and resources for cell-cell communication inference from single-cell RNA-Seq data. Nat Comms. 2022;13:3224–313.
30. Browaeys R, Saelens W, Saeys Y. NicheNet: modeling intercellular communication by linking ligands to target genes. Nat Methods. 2020;17:159–62.
31. Chen M-M, et al. Integrated single-cell and spatial transcriptomics uncover distinct cellular subtypes involved in neural invasion in pancreatic cancer. Cancer Cell. 2025;43:1656-1676.e10.
32. Arcila-Barrera S, et al. Acinar metaplastic cells generate semi-homogeneous niches and interact with immune cells. Gastroenterology. 2026;170:985–99.
33. Chen KH, Boettiger AN, Moffitt JR, Wang S, Zhuang X. RNA imaging. Spatially resolved, highly multiplexed RNA profiling in single cells. Science. 2015;348:aaa6090.
34. Brasel K, De Smedt T, Smith JL, Maliszewski CR. Generation of murine dendritic cells from flt3-ligand-supplemented bone marrow cultures. Blood. 2000;96:3029–39.
35. Kirkling ME, et al. Notch signaling facilitates in vitro generation of cross-presenting classical dendritic cells. Cell Rep. 2018;23:3658-3672.e6.
36. Helft J, et al. GM-CSF mouse bone marrow cultures comprise a heterogeneous population of CD11c(+)MHCII(+) macrophages and dendritic cells. Immunity. 2015;42:1197–211.
37. Daniel V, Sadeghi M, Wang H, Opelz G. CD4+CD25+Foxp3+IFN-γ+ human induced T regulatory cells are induced by interferon-γ and suppress alloresponses nonspecifically. Hum Immunol. 2011;72:699–707.
38. Feng T, Cao AT, Weaver CT, Elson CO, Cong Y. Interleukin-12 converts Foxp3+ regulatory T cells to interferon-γ-producing Foxp3+ T cells that inhibit colitis. Gastroenterology. 2011;140:2031–43.
39. Sawitzki B, et al. IFN-gamma production by alloantigen-reactive regulatory T cells is important for their regulatory function in vivo. J Exp Med. 2005;201:1925–35.
40. Fischer JC, et al. Tissue-adapted Tregs harness inflammatory signals to promote intestinal repair from therapy-related injury. Signal Transduct Target Ther. 2025;10:384.
41. Kerkar SP, et al. Timing and intensity of exposure to interferon-γ critically determines the function of monocyte-derived dendritic cells. Immunology. 2014;143:96–108.
42. Salmon H, et al. Expansion and activation of CD103(+) dendritic cell progenitors at the tumor site enhances tumor responses to therapeutic PD-L1 and BRAF inhibition. Immunity. 2016;44:924–38.
43. Minohara K, et al. Mature dendritic cells enriched in regulatory molecules may control regulatory T cells and the prognosis of head and neck cancer. Cancer Sci. 2023;114:1256–69.
44. Kim JM, Rasmussen JP, Rudensky AY. Regulatory T cells prevent catastrophic autoimmunity throughout the lifespan of mice. Nat Immunol. 2007;8:191–7.
45. Qureshi OS, et al. Trans-endocytosis of CD80 and CD86: a molecular basis for the cell-extrinsic function of CTLA-4. Science. 2011;332:600–3.
46. Bauer CA, et al. Dynamic Treg interactions with intratumoral APCs promote local CTL dysfunction. J Clin Invest. 2014;124:2425–40.
47. Rojas LA, et al. Personalized RNA neoantigen vaccines stimulate T cells in pancreatic cancer. Nature. 2023;618:144–50.
48. Sethna Z, et al. RNA neoantigen vaccines prime long-lived CD8+ T cells in pancreatic cancer. Nature. 2025;639:1042–51.
49. Kranz LM, et al. Systemic RNA delivery to dendritic cells exploits antiviral defence for cancer immunotherapy. Nature. 2016;534:396–401.

Publisher's Note Springer Nature remains neutral with regard to jurisdictional claims in published maps and institutional affiliations.

Authors and Affiliations

Yanyun Hao[1,2] · Oshri Yosefov-Levi[1] · Sebastian Arcila-Barrera[1] · Yehuda Shovman[1] · Avital Sarusi-Portuguez[3] · Vladyslav Holiar[4] · Hasan Burak Kunukcu[5,6] · Moshe Biton[4] · William L. Hwang[5,6] · Jinke Cheng[2] · Sharona Tornovsky-Babeay[1] · Oren Parnas[1]

✉ Oren Parnas
Oren.Parnas@gmail.com

1 The Concern Foundation Laboratories, The Lautenberg Center for Immunology and Cancer Research, Department of Immunology and Cancer Research-IMRIC, Faculty of Medicine, The Hebrew University of Jerusalem, Jerusalem, Israel

2 Department of Biochemistry and Molecular Cell Biology, Shanghai Key Laboratory for Tumor Microenvironment and Inflammation, Shanghai Jiao Tong University School of Medicine, Shanghai 200025, China

3 The Mantoux Bioinformatics Institute of the Nancy and Stephen Grand Israel National Center for Personalized Medicine, Weizmann Institute of Science, Rehovot, Israel

4 Department of Immunology and Regenerative Biology, Weizmann Institute of Science, Rehovot, Israel

5 Center for Systems Biology, Krantz Family Center for Cancer Research, Department of Radiation Oncology, Massachusetts General Hospital, Harvard Medical School, Boston, MA, USA

6 Broad Institute of MIT and Harvard, Cambridge, MA, USA